Soft Matter

PAPER

View Article Online
View Journal | View Issue

Cite this: *Soft Matter*, 2016, **12**, 2440

Dark-field differential dynamic microscopy†

Alexandra V. Bayles, Todd M. Squires and Matthew E. Helgeson*

Received 17th October 2015,
Accepted 22nd January 2016

DOI: 10.1039/c5sm02576a

www.rsc.org/softmatter

Differential dynamic microscopy (DDM) is an emerging technique to measure the ensemble dynamics of colloidal and complex fluid motion using optical microscopy in systems that would otherwise be difficult to measure using other methods. To date, DDM has successfully been applied to linear space invariant imaging modes including bright-field, fluorescence, confocal, polarised, and phase-contrast microscopy to study diverse dynamic phenomena. In this work, we show for the first time how DDM analysis can be extended to dark-field imaging, *i.e.* a linear space variant (LSV) imaging mode. Specifically, we present a particle-based framework for describing dynamic image correlations in DDM, and use it to derive a correction to the image structure function obtained by DDM that accounts for scatterers with non-homogeneous intensity distributions as they move within the imaging plane. To validate the analysis, we study the Brownian motion of gold nanoparticles, whose plasmonic structure allows for nanometer-scale particles to be imaged under dark-field illumination, in Newtonian liquids. We find that diffusion coefficients of the nanoparticles can be reliably measured by dark-field DDM, even under optically dense concentrations where analysis *via* multiple-particle tracking microrheology fails. These results demonstrate the potential for DDM analysis to be applied to linear space variant forms of microscopy, providing access to experimental systems unavailable to other imaging modes.

Introduction

Several techniques have been developed to measure passively and actively-driven dynamics in soft matter. On optical length scales, statistical analysis has been employed to infer particle dynamics from temporal and spatial intensity fluctuations of light directed at samples. Well-developed techniques include: multiple particle tracking microrheology (MPT),[1–3] particle image velocimetry (PIV),[4–6] diffusing wave spectroscopy (DWS),[7,8] fluorescence correlation spectroscopy (FCS),[9,10] and dynamic light scattering (DLS, also known as photon correlation spectroscopy).[11] Each of these techniques has its own advantages and disadvantages, making certain techniques better suited to measure specific material systems and dynamics than others.

Multiple particle tracking microrheology,[1–3] for example, is well-suited to measure dynamics of individual colloids in both heterogeneous and scarce materials. Particles between nanometers and microns in size can be directly visualized using different types of microscopy. From video micrographs, the position of particles can be determined to sub-pixel resolution by fitting different intensity masks over the micrograph and their dynamics correlated by tracking the centers as a function of time. It is possible to characterize spatially heterogeneous samples using MPT by examining particle movement at different locations within a micrograph.

Dynamic light scattering, on the other hand, is well-suited to measure average, ensemble dynamics across multiple length scales. In DLS, light from a collimated source is directed onto a sample and the light scattered at a particular angle θ (or wave vector $\mathbf{q}$) is recorded by a detector. Fluctuations in the scattered light arise when scatterers in the sample move within (and pass into and out of) the incident beam. Based on the time correlations of these fluctuations at different values of θ, it is possible to extract the dynamics of the scatterers at multiple length scales.

Unfortunately, neither MPT nor DLS are well-suited to measure the dynamics of dense samples. In MPT, particles have to be optically isolated to be tracked, limiting the use of MPT to samples with dilute, easily identified scatterer centers such as high-contrast tracer particles dispersed in a solvent. In DLS, multiple scattering convolutes intensity fluctuation correlations. DWS and fiber optic quasi-elastic light scattering can be used to overcome this limitation by directly analysing the multiply scattered light.[8,12] However, these techniques require specialized equipment that is not as common as that used for MPT or DLS.

Department of Chemical Engineering, University of California Santa Barbara, 3357 Engineering II, Santa Barbara, CA 93106, USA.
E-mail: helgeson@engineering.ucsb.edu; Fax: +1-805-893-4731; Tel: +1-805-893-3372

† Electronic supplementary information (ESI) available: Intensity profile additivity, sucrose solution viscosities, additional simulations, details of image structure function fitting procedure, dark-field image structure function at high magnification. See DOI: 10.1039/c5sm02576a

Recently, differential dynamic microscopy (DDM), a type of digital Fourier microscopy analysis,[13,14] was developed[15] based on the same principles of MPT and DLS. The technique measures sample dynamics by reconstructing dynamic scattering patterns from both temporal and spatial variations in micrograph image intensities. As a hybrid, DDM combines many of the advantages of MPT and DLS. Specifically, DDM (1) can characterize spatially heterogeneous and concentrated samples; (2) can extract dynamics from micrographs that bear little resemblance to the actual sample (*e.g.* weak scatterers or optically dense samples); (3) requires small sample volumes and (4) uses unmodified microscopes already present in most academic and industrial labs. With this unique combination of advantages, DDM has great potential to complement existing techniques like DLS and MPT that are widely used to characterize soft matter. As such, it is worthwhile to further develop different aspects of DDM, and, in particular, extend it to different forms of microscopy as we endeavour to do here.

Before describing our contribution to the development of DDM, we provide an overview of the mechanics of the technique and the current state of the DDM field. Those interested in a more detailed description can refer to a recent review article by Giavazzi and Cerbino.[13] DDM was first developed to measure the dynamics of colloidal and complex fluid motion using intensity fluctuations of simple video micrographs.[15] From DDM, it is possible to obtain the same autocorrelation function measured in dynamic light scattering as a function of wave vector ($\mathbf{q}$) space in systems that are not compatible with DLS, and using smaller sample volumes. Since its original development, DDM has been successfully used to measure particle diffusivity,[16] particle velocity,[17] colloidal aggregation and gelation kinetics,[18,19] bacterial motility,[20–23] hydrodynamic factors in concentrated colloidal dispersions,[21] viscoelasticity of liquid crystals,[24] and anisotropic particle motion.[25] It has also been adapted for use in texture analysis microscopy.[26]

Much like in MPT, the first step of DDM is to collect a series of images of material in motion using a microscope. The video micrograph series is analysed by first computing the change in intensity of each pixel $I(\mathbf{x},t)$ between two micrographs separated by time step Δt. The 2D Fourier transform of the resulting difference image $\Delta\hat{I}(\mathbf{q},\Delta t)$ is a convolution of the visual representation of scattering centers and the displacement of scattering centers over Δt. It is possible to decouple these two contributions by analyzing the expectation value of the Fourier power spectrum of the difference images, defined as the dynamic image structure function, $D(\mathbf{q},\Delta t)$

$$D(\mathbf{q},\Delta t) \equiv \langle |\Delta\hat{I}(\mathbf{q},\Delta t)|^2 \rangle \quad (1)$$

In a seminal text, Giavazzi and coworkers showed that in linear space invariant forms of microscopy (which will be discussed shortly), the dynamic image structure function decomposes analytically into three sub-functions:[27]

$$D(\mathbf{q},\Delta t) = A(\mathbf{q})[1 - g(\mathbf{q},\Delta t)] + B(\mathbf{q}) \quad (2)$$

In eqn (2), the function $A(\mathbf{q})$ is a convolution of the particle scattering properties, the optical transfer function of the imaging optics, and the material structure factor. $B(\mathbf{q})$ is related to the imaging noise and incoherent scattering. For uncorrelated image noise, $B(\mathbf{q})$ is a constant that is independent of q. In the analysis below, we will show that $g(\mathbf{q},\Delta t)$, is equivalent to the intensity autocorrelation function measured by DLS.

In systems where scatterer motion is spatially isotropic (*e.g.* Brownian motion), radially symmetric scattering patterns are produced if averaged over a sufficiently large time. In such cases, the dynamic image structure function is radially averaged and subsequently analysed in terms of two independent variables, Δt and q, the magnitude of the wavevector $\mathbf{q}$. The image structure function $D(q,\Delta t)$ can be fit to eqn (2) for lines of constant q provided that a suitable model for $g(q,\Delta t)$ can be can be found for a particular material system. In addition to $A(q)$ and $B(q)$, this provides wave vector dependent values of the parameters chosen in the model for $g(q,\Delta t)$. For instance, in the case where the intensity autocorrelation function decays according to

$$g(q,\Delta t) = e^{-\Delta t/\tau(q)} \quad (3)$$

q dependent values of τ are obtained.

To date, differential dynamic analysis has been successfully applied to bright-field,[16–19,22,28] fluorescence,[16] confocal,[21] polarised,[24] and phase-contrast[20,23,25] forms of microscopy. One widely used imaging mode that is not included in this list is dark-field microscopy, the illumination system for which is depicted in Fig. 1a. In dark-field microscopy, direct light is blocked such that only the light scattered by the sample enters the objective and is recorded by the camera. This form of illumination provides a better signal-to-noise ratio in many samples with strong scattering but insufficient contrast to be observed in other imaging modes. For example, dark-field microscopy is commonly used to image unstained biological samples,[29–31] crystal grain boundaries,[32] and nanoparticles.[33] Fig. 1b shows the enhanced signal obtained using dark-field microscopy to image gold nanoparticles compared to bright-field imaging, in this case due to the strong surface plasmon resonance of the nanoparticles.[34] Since dark-field microscopy provides a better signal-to-noise ratio for specific soft matter classes than other illumination systems, applying DDM to dark-field micrographs instead of poorer images obtained in other illumination systems has the potential to yield high quality dynamic statistics, as well as applicability to material systems that are incompatible with other imaging modes. This is illustrated in Fig. 1d where we measure the image structure function from dark-field and bright-field micrographs of dilute 100 nm Au nanoparticles undergoing Brownian motion in aqueous sucrose solutions. The dark-field image structure function has a strong exponential dependence, allowing for precise measurement of $\tau(q)$, whereas the bright-field image structure function is essentially just a measurement of the camera noise.

Differential dynamic analysis has not yet been applied to dark-field micrographs because dark-field is a linear space

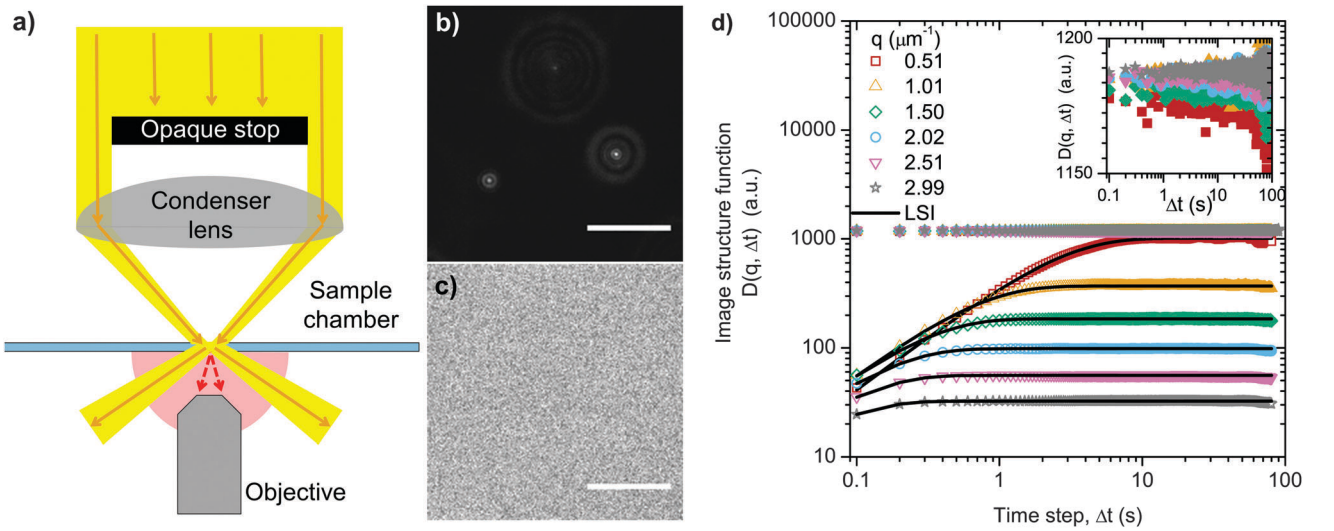

Fig. 1 Higher signal-to-noise ratio in dark-field imaging yields improved DDM statistics. (a) In dark-field illumination, light that is normally incident directly on the objective is blocked by an opaque stop. The remaining light is focused on the sample using a condenser lens. Light scattered by the sample is captured by the objective, while the direct light is outside of the objective view. (b) Dark-field and (c) bright-field micrographs of 100 nm Au nanoparticles dispersed in a Newtonian fluid (30 wt% sucrose solution) at $\phi = 5.4 \times 10^{-8}$. Due to surface plasmon resonance, Au nanoparticles scatter large amounts of light, which is recorded well using dark-field microscopy. Comparison of the dark-field and bright-field micrographs shows the higher fidelity of dark-field imaging. Scale bars are 10 μm. (d) Image structure function of the Au nanoparticle dispersion imaged under dark-field microscopy (open symbols) and bright-field microscopy (closed symbols). Experimental dark-DDM image structure function fits well to the linear space invariant decomposition, eqn (6). Inset shows that the bright-DDM image structure function exhibits no exponential time dependence other than the increased spread at long times, which reflects that fewer difference images contribute to the ensemble average at long times.

variant (LSV) imaging system. In linear space variant illumination systems, the intensity distribution projected by a scatterer onto a micrograph varies as the scatterer traverses the x–y sample plane. This effect is captured in Fig. 2.

The sub-function decomposition derived by Giavazzi *et al.*[27] (eqn (2)) and employed in nearly every subsequent application of DDM begins by assuming that the illumination system is linear space invariant. Specifically, the micrograph intensity at time t, $I(\mathbf{x},t)$ is described according to the Nemoto–Streibl model of imaging optics[35,36]

$$I(\mathbf{x},t) = I_0 + \iiint d\mathbf{x}' dz' K(\mathbf{x}-\mathbf{x}', -z') c(\mathbf{x}', z', t) \qquad (4)$$

In eqn (4), I_0 is the background intensity, and $\mathbf{x}'$ and z' are coordinates within the three dimensional sample. $K(\mathbf{x}-\mathbf{x}', -z')$ is the optical transfer function, and $c(\mathbf{x}', z', t)$ is the concentration distribution of the scatterers. Implicit in the kernel of eqn (4) is that the described illumination system is linear space invariant. That is, a scatterer's intensity profile remains the same when the scatterer moves in $\mathbf{x}'$.

We hypothesize that DDM can still provide valuable information about fluid dynamics in dark-field imaging despite its linear space variance (this is already suggested by the data presented in Fig. 1d). In a recent review, Giavazzi and Cerbino[13] suggested this although it has not been verified experimentally or theoretically. In this work, we demonstrate the opportunities and limitations of using DDM (and other linear space variant illuminations systems) using theory, simulations and experiments. Specifically, we revisit the original theoretical justification of DDM analysis[27] developed from the point-spread function of a microscope. Since it is difficult, if not impossible in many cases, to measure a linear space variant microscope's point-spread function, we recast the theoretical development in terms of the displacements of scatterers that project arbitrary intensity profiles in the micrograph plane. We simulate micrographs of particles undergoing 2D random walks in LSV imaging systems. Finally, we verify this analysis by measuring the dynamics of nanoparticle suspensions in different Newtonian fluids.

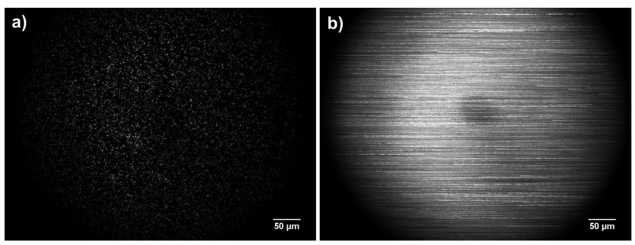

Fig. 2 Linear space variance in dark-field microscopy. (a) Dark-field micrograph of 100 nm Au nanoparticles deposited on a glass slide. The same glass slide is imaged under dark-field as it is translated horizontally. (b) Compilation of the translated images, *i.e.* the trajectories of the particles, as they move in (x) but remain at a constant (y,z). Intensity variation across the image is primarily due to linear space variance.

Theory

Our objective here is to provide a framework for determining the mechanism by which the LSI DDM formalism fails in LSV

forms of microscopy. As an archetypal case study, we consider Brownian motion of non-interacting scatterers in a Newtonian fluid. Readers interested in system with more complicated dynamics (*e.g.* non-Newtonian dispersions, concentrated dispersions, *etc.*) can use the same theoretical approach to determine regimes where standard LSI analysis holds.

Brownian motion of generic scatterers in linear-space invariant systems: a scatterer displacement approach

Consider a 2D micrograph taken of a sample containing scatterers in motion. Let $I(\mathbf{x},t)$ be the intensity of the micrograph at the position $\mathbf{x}$ at a particular time t. After some time step Δt, the scatterers in the sample move to a new position and the background intensity $i_B(\mathbf{x},t)$ fluctuates due to noise in the detector and illumination source.

The change in intensity after Δt is simply $\Delta I(\mathbf{x},\Delta t) = I(\mathbf{x},t+\Delta t) - I(\mathbf{x},t)$. Statistical analysis of the time-dependent differences in intensity gives information about the dynamics of the sample. The expectation value of the Fourier power spectrum of $\Delta I(\mathbf{x},\Delta t)$ is defined as the image structure function, $D(\mathbf{q},\Delta t)$[15]

$$D(\mathbf{q},\Delta t) \equiv \langle |\Delta \hat{I}(\mathbf{q},\Delta t)|^2 \rangle \tag{5}$$

The image structure function contains information about movement of the scatterers, their contribution to changing the micrograph intensity, and fluctuations in the background intensity. As shown by Giavazzi and Cerbino *et al.*,[27] it is possible to deconvolute these contributions in LSI imaging systems. The image structure function can thus be broken into three independent functions:

$$D(\mathbf{q},\Delta t) = A(\mathbf{q})[1 - g(\mathbf{q},\Delta t)] + B(\mathbf{q}) \tag{6}$$

To explicitly relate these functions and the physical system, we will consider the system in terms of a generic intensity profile projected by scatterers onto the micrograph. Let the total intensity of each image be the sum of the signals produced by scatterers in the sample plane, $i_S(\mathbf{x},t)$ and the background intensity, $i_B(\mathbf{x},t)$

$$I(\mathbf{x},t) = i_S(\mathbf{x},t) + i_B(\mathbf{x},t) \tag{7}$$

Let us assume the intensity profile of a single scatterer is not influenced by other scatterers. As such, the analysis can be limited to a single scatterer that, when centered at the origin, projects an intensity profile $i_{LSI}(\mathbf{x})$ onto the plane of the micrograph. In this case, the total micrograph intensity is $I(\mathbf{x},t) = i_{LSI}(\mathbf{x},t) + i_B(\mathbf{x},t)$. Time manifests as a change in location of the scatterer center to a position $\mathbf{x_i}$. In LSI imaging systems, the functional form of the intensity profile does not change as the scatterer moves within the sample plane. Consequently, the scatterer's intensity profile can be written in terms of the shift $\mathbf{x} - \mathbf{x_i}(t)$ and the total micrograph intensity becomes

$$I(\mathbf{x},t) = i_{LSI}(\mathbf{x} - \mathbf{x_i}(t)) + i_B(\mathbf{x},t) \tag{8}$$

The Fourier transform of the micrograph intensity is

$$\hat{I}(\mathbf{q},t) = \mathrm{FT}[i_{LSI}(\mathbf{x} - \mathbf{x_i}(t)) + i_B(\mathbf{x},t)] = \hat{i}(\mathbf{q})e^{-j\mathbf{x_i}(t)\cdot\mathbf{q}} + \hat{i}_B(\mathbf{q},t) \tag{9}$$

where $\hat{i}(\mathbf{q})$ is the Fourier transform of $i_{LSI}(\mathbf{x} - \mathbf{x_i}(t))$ when the scatterer is centered at the origin. Let the scatterer be centered at $\mathbf{x}_0$ at t. After a time Δt, the scatterer moves to position $\mathbf{x}_1$, for a displacement $\delta\mathbf{x} = \mathbf{x}_1 - \mathbf{x}_0$. The resulting change in micrograph intensity is

$$\Delta\hat{I}(\mathbf{q},\Delta t) = \hat{i}(\mathbf{q})(e^{-j\mathbf{q}\cdot\mathbf{x}_1} - e^{-j\mathbf{q}\cdot\mathbf{x}_0}) + \hat{i}_B(\mathbf{q},t+\Delta t) - \hat{i}_B(\mathbf{q},t) \tag{10}$$

The image structure function is determined by finding the expectation value of the square modulus of the change in intensity, $\Delta\hat{I}^*(\mathbf{q},\Delta t)\Delta\hat{I}(\mathbf{q},\Delta t)$. Analytically, the expectation value of the quantity$\cdots$is defined as

$$\langle \cdots \rangle = \langle \langle \cdots \rangle_t \rangle_V \tag{11}$$

The symbol $\langle \cdots \rangle_t$ denotes the average over time

$$\langle \cdots \rangle_t = \int_{-\infty}^{\infty} \mathrm{d}(\delta\mathbf{x})[p(\delta\mathbf{x},\Delta t)\cdots] \tag{12}$$

where $p(\delta\mathbf{x},\Delta t)$ is the probability that the scatterer will move by an amount $\delta\mathbf{x}$ during the time Δt. The functional form of $p(\delta\mathbf{x},\Delta t)$ varies depending on the dynamics of the scatterers. For the archetypal case of 2D Brownian motion of dilute, non-interacting scatterers, $p(\delta\mathbf{x},\Delta t)$ is

$$p(\delta\mathbf{x},\Delta t) = (4\pi D_{Self}\Delta t)^{-1} e^{-\delta\mathbf{x}^2/4D_{Self}\Delta t} \tag{13}$$

where D_{Self} is the self-diffusivity of the scatterer.[37] Study of more complex systems (*e.g.* concentrated suspensions) requires replacement of $p(\delta\mathbf{x},\Delta t)$ with an appropriate probability distribution. The symbol $\langle \cdots \rangle_V$ denotes the average over the sample volume

$$\langle \cdots \rangle_V = \int_{-l_x}^{l_x} d(x_0) \int_{-l_y}^{l_y} d(y_0)[p(x_0,y_0)\cdots] \tag{14}$$

where l_x and l_y are the dimensions of the sample volume imaged. For the case of a uniform initial distribution of scatterers, $p(x_0,y_0)$ is

$$p(x_0,y_0) = \frac{1}{4l_x l_y} \tag{15}$$

Combining eqn (10)–(15) gives

$$\langle |\Delta\hat{I}(\mathbf{q},\Delta t)|^2 \rangle = 2\langle |\hat{i}(\mathbf{q})|^2 \rangle [1 - e^{-\Delta t/\tau(q)}] + \langle |\Delta\hat{i}_B(\mathbf{q},\Delta t)|^2 \rangle \tag{16}$$

The material relaxation time τ is equal to

$$\tau(q) = \frac{1}{q^2 D_{Self}} \tag{17}$$

Comparing eqn (16) to eqn (6), we see that the three independent functions are

$$A(\mathbf{q}) = 2\langle |\hat{i}(\mathbf{q})|^2 \rangle \tag{18}$$

$$g(\mathbf{q},\Delta t) = e^{-\Delta t/\tau(q)} \tag{19}$$

$$B(\mathbf{q}) = \langle |\Delta\hat{i}_B(\mathbf{q},\Delta t)|^2 \rangle \tag{20}$$

In eqn (18)–(20) $A(\mathbf{q})$ depends only on the intensity profile of the scatterer, $g(\mathbf{q},\Delta t)$ depends only on the dynamics of the scatterer, and $B(\mathbf{q})$ is solely related to the background fluctuations.

Note that $B(\mathbf{q})$ is not an explicit function of Δt since the fluctuations in the background are assumed to be random on the time scale of Δt. We also note that if we consider a system of N scatterers with additive intensity profiles as done by Reufer *et al.*,[25] $A(q) = 2\langle|\hat{i}(\mathbf{q})|^2\rangle NS(q)$. $S(q)$ is the static structure factor of the material, which is equal to 1 for simple dilute dispersion of scatterers in a Newtonian fluid. Under the physically dilute conditions studied here, we find that it is reasonable to assume intensity profiles are additive (see Fig. S1 and S2, ESI†).

It is useful to analyse the empirically obtained $D(\mathbf{q},\Delta t)$ signal in terms of eqn (6). In practice, the signal $D(\mathbf{q},\Delta t)$ is first radially averaged in $\mathbf{q} = (q_x,q_y)$ space such that it is a function of the scalar q, where $q = (q_x^2 + q_y^2)^{1/2}$. Then, each curve of constant wavevector, q, in $D(q,\Delta t)$ is fit as a function of time such that there are three independent parameters, A, τ and B. Doing so allows the structure relaxation time $\tau(q)$ to be extracted without prior knowledge of the functional form of $A(q)$. In the following section, we demonstrate how the same analytical approach can be used to analyse LSV micrographs within specified experimental limits.

Brownian motion of generic scatterers in linear space variant systems

Here, we use the same scatterer displacement approach to derive a decomposed form of the image structure function in LSV imaging systems. Specifically, we show that in LSV systems, the image structure function can be approximated as

$$D(\mathbf{q},\Delta t) \approx A(\mathbf{q})[1 - g(\mathbf{q},\Delta t) + V(\mathbf{q},\Delta t)] + B(\mathbf{q}) \quad (21)$$

Again, let the total intensity of each image be the sum of the signal produced by scatterers in the sample plane, $i_S(\mathbf{x},t)$ and the background intensity, $i_B(\mathbf{x},t)$ as written in eqn (7). Let us then assume that a scatterer centered at the origin of the sample projects an intensity profile, $i_{LSV}(\mathbf{x})$, onto the plane of the micrograph. In this case, the micrograph's intensity will be $I(\mathbf{x},t) = i_{LSV}(\mathbf{x},t) + i_B(\mathbf{x},t)$. As in the LSI imaging system, time manifests as a change in position of the scatterer center, $\mathbf{x}_i$. However, in the LSV imaging system, the scatterer's intensity profile changes as it moves within the sample plane. In many LSV imaging systems, it is the absolute intensity of the intensity profile, but not the functional form, that changes as the object shifts, as depicted in Fig. 3. In such a system, the intensity profile can be approximated by an absolute intensity multiplicative factor, $\alpha(\mathbf{x}_i)$, altering the space invariant functional form, $i_{LSI}(\mathbf{x} - \mathbf{x}_i(t))$:

$$i_{LSV}(\mathbf{x},t) = \alpha(\mathbf{x}_i) i_{LSI}(\mathbf{x} - \mathbf{x}_i(t)) \quad (22)$$

As such, the total micrograph intensity is

$$I(\mathbf{x},t) = \alpha(\mathbf{x}_i) i_{LSI}(\mathbf{x} - \mathbf{x}_i(t)) + i_B(t) \quad (23)$$

The Fourier transform of the micrograph intensity is

$$\begin{aligned}\hat{I}(\mathbf{q},t) &= \mathrm{FT}[i_{LSV}(\mathbf{x} - \mathbf{x}_i(t)) + i_B(\mathbf{x},t)] \\ &= \alpha(\mathbf{x}_i)\hat{i}_{LSI}(\mathbf{q})e^{-j\mathbf{x}_i(t)\cdot\mathbf{q}} + \hat{i}_B(\mathbf{q},t)\end{aligned} \quad (24)$$

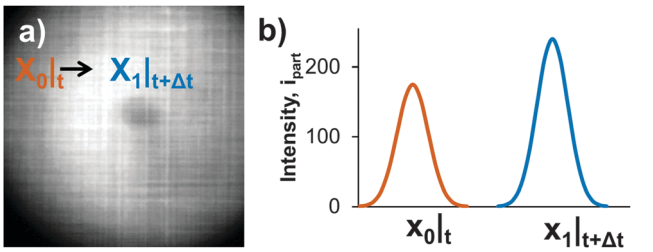

Fig. 3 Mathematical approximation used for linear space variance. (a) Dark-field micrograph of Au nanoparticles traversing the (x,y) plane illustrates the spatial dependence of the magnitude of the intensity profile. (b) Magnitude of Gaussian intensity profile changes as scatterers move in $\mathbf{x}$.

where $\hat{i}_{LSI}(\mathbf{q})$ is the Fourier transform of the LSI portion when the object is centered at the origin. Let the scatterer be centered at $\mathbf{x}_0$ at t. After a time Δt, the scatterer moves to position $\mathbf{x}_1$, for a displacement $\delta\mathbf{x} = \mathbf{x}_1 - \mathbf{x}_0$. The resulting change in micrograph intensity is

$$\Delta\hat{I}(\mathbf{q},\Delta t) = \hat{i}_{LSI}(\mathbf{q})(\alpha(\mathbf{x}_1)e^{-j\mathbf{q}\cdot\mathbf{x}_1} - \alpha(\mathbf{x}_0)e^{-j\mathbf{q}\cdot\mathbf{x}_0}) + \hat{i}_B(\mathbf{q},t + \Delta t) - \hat{i}_B(\mathbf{q},t) \quad (25)$$

Ensemble averaging of $\Delta\hat{I}(\mathbf{q},\Delta t)$ will eventually involve integration of $\alpha(\mathbf{x}_i)$. To do so without *a priori* knowledge of its functional form, we employ a Taylor expansion to approximate changes in $\alpha(\mathbf{x}_i)$

$$\alpha(\mathbf{x}_1) \approx \alpha(\mathbf{x}_0) + (\mathbf{x}_1 - \mathbf{x}_0)\cdot\nabla\alpha|_{\mathbf{x}_0} + O((\delta\mathbf{x}\cdot\nabla)^2\alpha) \quad (26)$$

$$\alpha(\mathbf{x}_1) \approx \alpha(\mathbf{x}_0) + (\delta\mathbf{x})\cdot\nabla\alpha|_{\mathbf{x}_0} + O((\delta\mathbf{x}\cdot\nabla)^2\alpha) \quad (27)$$

where $O((\delta\mathbf{x}\cdot\nabla)^2\alpha)$ denotes higher order terms. Substituting the Taylor expansion into eqn (25) gives

$$\begin{aligned}\Delta i(\mathbf{q},\Delta t) \approx{}& \hat{i}_{LSI}(\mathbf{q})(\alpha(\mathbf{x}_0)(e^{-j\mathbf{q}\cdot\mathbf{x}_1} - e^{-j\mathbf{q}\cdot\mathbf{x}_0}) + (\delta\mathbf{x})\cdot\nabla(\alpha)|_{\mathbf{x}_0}e^{-j\mathbf{q}\cdot\mathbf{x}_1}) \\ &+ \hat{i}_B(\mathbf{q},t + \Delta t) - \hat{i}_B(\mathbf{q},t) + O((\delta\mathbf{x}\cdot\nabla)^2\alpha)\end{aligned} \quad (28)$$

The image structure function is determined by finding the expectation value of the square modulus of the change in intensity, $\Delta\hat{I}^*(\mathbf{q},\Delta t)\Delta\hat{I}(\mathbf{q},\Delta t)$ and employing eqn (10)–(15). Doing so gives

$$\begin{aligned}\left\langle|\Delta\hat{I}(\mathbf{q},\Delta t)|^2\right\rangle \approx{}& 2\left\langle\alpha(\mathbf{x}_0)^2\right\rangle\left\langle|\hat{i}(\mathbf{q})|^2\right\rangle\left[1 - e^{-\Delta t/\tau(q)}\right] \\ &+ 2\left\langle\alpha(\mathbf{x}_0)^2\right\rangle\left\langle|\hat{i}(\mathbf{q})|^2\right\rangle\frac{\left\langle\left(\nabla\alpha|_{\mathbf{x}_0}\right)^2\right\rangle}{\left\langle\alpha(\mathbf{x}_0)^2\right\rangle}D_{Self}\Delta t \\ &+ \left\langle|\Delta\hat{i}_B(\mathbf{q},\Delta t)|^2\right\rangle + O\left(\left[(\delta\mathbf{x}\cdot\nabla)^2\alpha\right]^2\right)\end{aligned} \quad (29)$$

where $\langle\alpha(\mathbf{x}_0)^2\rangle$ is the average square magnitude of the intensity amplitude, α, of scatterers over the micrograph and $\langle(\nabla\alpha|_{\mathbf{x}_0})^2\rangle$ is the average square of the magnitude of the gradient of the intensity over the micrograph. The term $\frac{\left\langle\left(\nabla\alpha|_{\mathbf{x}_0}\right)^2\right\rangle}{\left\langle\alpha(\mathbf{x}_0)^2\right\rangle}$ quantifies the first effect of the degree of linear space variance in an

illumination system. We define a new variable, χ, as the linear field variance factor:

$$\chi \equiv \left(\frac{\left\langle \left(\nabla \alpha|_{\mathbf{x}_0} \right)^2 \right\rangle}{\left\langle \alpha(\mathbf{x}_0)^2 \right\rangle} \right)^{1/2} \tag{30}$$

Comparing eqn (29) to eqn (21), we see that the four independent functions in the LSV decomposition are

$$A(\mathbf{q}) = 2\langle \alpha(\mathbf{x}_0)^2 \rangle \langle |\hat{i}(\mathbf{q})|^2 \rangle \tag{31}$$

$$g(\mathbf{q},\Delta t) = \mathrm{e}^{-\Delta t/\tau(q)} \tag{32}$$

$$B(\mathbf{q}) = \langle |\Delta \hat{i}_{\mathrm{B}}(\mathbf{q},\Delta t)|^2 \rangle \tag{33}$$

$$V(\mathbf{q},\Delta t) = \chi^2 D_{\mathrm{Self}} \Delta t \tag{34}$$

Examining these equations, it is clear that $A(\mathbf{q})$, $g(\mathbf{q},\Delta t)$ and $B(\mathbf{q})$ have the same physical dependence as they did in the LSI imaging system. The additive LSV correction, $V(\mathbf{q},\Delta t)$ accounts for the effects of linear space variance, and is shown here for the case of Brownian motion of dilute scatterers. To determine $V(\mathbf{q},\Delta t)$ for more complex dynamics, one would need to employ a different equation for $p(\delta \mathbf{x},\Delta t)$ in the framework developed here.

For the case of Brownian motion, $V(\mathbf{q},\Delta t)$ depends on two parameters, χ and D_{Self}. Casting the image structure function in terms of dimensionless quantities shows the relative effect of $V(\mathbf{q},\Delta t)$ on $D(\mathbf{q},\Delta t)$ across all possible experimental parameters (q, set by the magnification and Δt set by the frame rate). Fig. 4 plots the normalized LSV image structure function

$$\frac{\left\langle \left| \Delta \hat{I}(\mathbf{q},\Delta t) \right|^2 \right\rangle}{2\left\langle \alpha(\mathbf{x}_0)^2 \right\rangle \left\langle \left| \hat{i}(\mathbf{q}) \right|^2 \right\rangle} \approx 1 - \mathrm{e}^{-\Delta t q^2 D_{\mathrm{Self}}} + \left(\frac{\chi}{q} \right)^2 \Delta t q^2 D_{\mathrm{Self}} \tag{35}$$

as a function of dimensionless time $\Delta t q^2 D_{\mathrm{Self}}$ with $B(\mathbf{q}) = 0$. We see that the LSV image structure can be physically understood

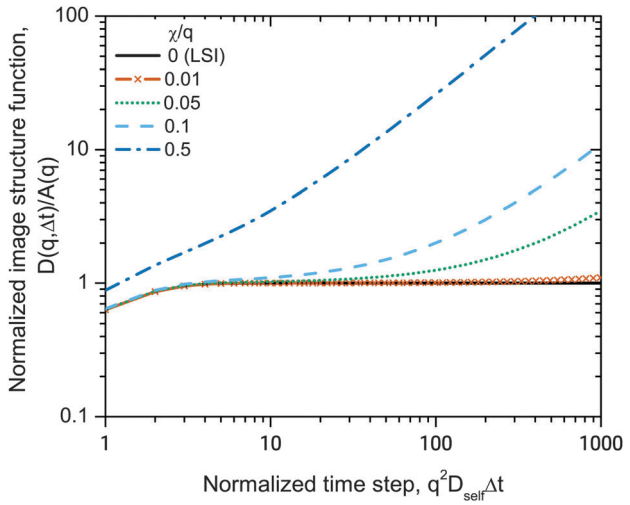

Fig. 4 The theoretical image structure function for scatterers undergoing Brownian motion in linear space variant imaging systems. Deviation from the linear space invariant case (solid black line) increases with increasing magnitude of space variance, quantified by the factor χ normalized by q.

in terms of two time scales, the material relaxation time $\tau(q)$ and the so called LSV time scale τ_{LSV}, which is the characteristic time required for the scatterer to experience a significant change in intensity due to the LSV field gradient. For the case of Brownian motion, these time scales are $(q^2 D_{\mathrm{Self}})^{-1}$ and $(\chi^2 D_{\mathrm{Self}})^{-1}$ respectively. The value of the image structure function at any time step will be the sum of intensity differences due to pure scatterer displacement and due to intensity variation across the field. When $\Delta t \ll \tau(q)$, the normalized image structure function approaches

$$\frac{\left\langle \left| \Delta \hat{I}(\mathbf{q},\Delta t) \right|^2 \right\rangle}{2\left\langle \alpha(\mathbf{x}_0)^2 \right\rangle \left\langle \left| \hat{i}(\mathbf{q}) \right|^2 \right\rangle} \sim \frac{\Delta t}{\tau(q)} \left(1 + \left(\frac{\chi}{q} \right)^2 \right) \tag{36}$$

when $\chi \ll q$ linear space variance does not contribute significantly to the image structure function, and the LSI decomposition should fit the experimental LSV image structure function at very short times. This implies that the shortest q (*i.e.* the longest distance) that can be accurately fit to the LSI decomposition is limited by gradient in $\alpha(\mathbf{x}_i)$.

On the other hand, when $\Delta t \gg \tau(q)$, the normalized image structure function approaches

$$\frac{\left\langle \left| \Delta \hat{I}(\mathbf{q},\Delta t) \right|^2 \right\rangle}{2\left\langle \alpha(\mathbf{x}_0)^2 \right\rangle \left\langle \left| \hat{i}(\mathbf{q}) \right|^2 \right\rangle} \sim 1 + \left(\frac{\chi}{q} \right)^2 \frac{\Delta t}{\tau(q)} \sim 1 + \chi^2 D_{\mathrm{Self}} \Delta t \tag{37}$$

At long times, there are significant deviations from the LSI image structure function when $\Delta t \sim (\chi^2 D_{\mathrm{Self}})^{-1}$ or larger. In our experimental system, $\chi/q \leq 0.01$. Referring back to Fig. 4, the contribution from LSV at this ratio is nearly imperceivable, particularly if one were to consider noise in a real experimental system. Furthermore, at this ratio the contribution from LSV should be less than the contribution due to intensity changes when the particle moves into and out of the focal plane. 3D motion can cause a change not only in the magnitude of the scatterer intensity, but also the spread or fringe spacing of the profile. In LSI systems, the error associated with neglecting contributions due to 3D motion are frequently assumed to be negligible.[27] Considering all of these factors, fitting empirical image structure functions to the LSI decomposition eqn (6) and the LSV decomposition should give identical measures of the diffusivity within acceptable margins of error.

This analysis indicates that it is practically reasonable to use the LSI decomposition to analyse LSV micrographs when $q \gg \chi$. It is advantageous to use the LSI decomposition over the LSV decomposition since the LSI decomposition does not require a measurement of the value of χ *a priori*. We test this claim using simulations and experiments described in the next section.

Experimental

Simulated micrographs

2D random walk trajectories were computed in MATLAB, and simulated particle intensities were generated in both LSI and LSV imaging systems. Random walk trajectories were simulated by first initializing 49 point particles on a square lattice within

a 490 × 490 pixel^2 space. For each time step, a new particle coordinate was determined by selecting the direction from a random number generator and selecting the length of the diffusion step by sampling a Gaussian distribution of displacements. The Gaussian distribution was based on a self-diffusivity of 0.5 pixel^2 per frame.

To form each micrograph, the intensity over the 490 × 490 pixel^2 space was calculated by centering a 2D Gaussian beam at each of the particle centers. The magnitude of the Gaussian beam, α, varies according to the location of the particle center $\mathbf{x}_i$ depending on the illumination system being simulated. Explicitly, a particle centered at $\mathbf{x}_i$ produces the intensity profile

$$i_{\mathrm{Gauss}}(\mathbf{x}|\mathbf{x}_i) = \alpha(\mathbf{x}_i)\exp\left(\frac{-(\mathbf{x}-\mathbf{x}_i)^2}{2\sigma^2}\right) \qquad (38)$$

where $\alpha(\mathbf{x}_i)$ is the magnitude of the Gaussian profile as a function of particle center, $\mathbf{x}_i$, and σ is the standard deviation of the Gaussian. Noise was not added to the intensity distributions nor to the background of the image. These simulated intensity distributions were saved as images and analysed using the same DDM algorithm described in the Image processing section. To be consistent with the experiments conducted, each simulated micrograph series was 900 frames long. The physical duration of the simulations were varied by changing the sampling interval. Simulations that mimic the real experiments were sampled at Δt = 1 frame; simulations that are 10× as long as an experiment were sampled at Δt = 10 frames.

Gold nanoparticle dispersion sample preparation

Three Newtonian fluids comprised of aqueous sucrose solutions were prepared at 29.92, 40.05 and 50.03 wt% sucrose (EMB Millipore) in deionized H_2O. Hereafter we refer to these solutions as 30 wt%, 40 wt%, and 50 wt% respectively. The viscosities of the solutions (see Fig. S3, ESI†) were measured using an Anton Paar vibrational density meter with an inline falling ball viscometer (DMA 4100 M). Citrate capped gold nanoparticles (TEM diameter: 94.6 ± 12.5 nm) were purchased from NanoComposix, Inc. and used without further modification. To prepare optically dilute samples, nanoparticles were dispersed in the three sucrose solutions at 5.4 × 10^{-6} vol% gold. For the optically dense sample, nanoparticles were dispersed in a different 50.00 wt% sucrose at 3.2 × 10^{-3} vol% gold. At these low volume fractions, it is reasonable to assume that both the optically dilute and optically dense dispersions are physically dilute and that hydrodynamic interactions between particles can be neglected.

Sample chambers for microscopy studies were fabricated from glass slides and UV-initiated thiolene resin (Norland Optical Adhesive, No. 81). Two glass spacers were first cut from a cover glass slide (Fisherbrand 24 × 50 mm − 1.5) to be ∼5 mm in width. Thiolene resin was then applied on one side of two separate spacers, and the spacers were set on a 25 × 75 × 1 mm microslide (Gold Seal), which serves as the top of the chamber. The spacers were positioned such that there was 25 mm between them. The spacers and the glass slide were then exposed to ultraviolet light (Spectroline™, Model XX15A, λ = 365 nm) for ∼30 s. After the initial exposure, a line of resin was applied to each of the top spacers and between the spacer columns on one side. A coverslip (Fisher Scientific, 22 × 50 − 1) was positioned on top of the spacers, and the entire chamber cured for 5 minutes. The Au nanoparticle dispersions were introduced through the remaining open side of the chamber and sealed with the UV resin, forming an airtight glass chamber.

Dark-field and bright-field microscopy

A representative schematic of the dark field illumination system is found in Fig. 1a. In the dark-field illumination system used here, an inverted microscope (Olympus 1 × 71) was outfit with a high-resolution dark-field condenser illumination adapter (CytoViva). The adapter contains an opaque stop that blocks direct light from the illumination source and a condenser that focuses the remaining light on the sample. Light scattered by the sample was captured by 10× and 40× air objectives (NA 0.25 and 0.75 respectively). Videos (512 × 512 pixels^2) of the motion of the Au nanoparticles were recorded using an Andor Clara CCD camera at 10.001 frames per second and an exposure time of 1 ms. Videos were 900 frames in length and recorded as multipage TIF files. The ambient temperature was measured using a Fisher Scientific traceable thermometer throughout the experiments.

The magnitude of the particle intensity profile as a function of space was experimentally approximated by depositing 100 nm Au nanoparticles on a glass slide. A dark-field micrograph video was recorded as the glass slide was translated horizontally and vertically. Projecting the maximum local intensity of each frame of the micrograph video (*i.e.* the center of each intensity profile) gave the field variance (see Fig. 2b). Smoothing this image using ImageJ software gave an approximate measurement of $\alpha(\mathbf{x}_i)$ (see Fig. 3a). The measured value of χ in the smoothed micrograph was 1.4 × 10^{-2} μm^{-1}, which is artificially high since the particle trajectories produce streaking that is not representative of the true value of $\alpha(\mathbf{x}_i)$. Nevertheless, the measurement provides an extreme maximum bound on the value of χ.

Bright-field micrographs were recorded using identical exposure, resolution, frame rate and magnification settings as used for the dark-field micrographs.

Image processing

A DDM analysis algorithm was written and executed in MATLAB.[38] Each video was first separated into individual frames. Frames separated by time step Δt were subtracted from one another, and the resulting difference image was fast Fourier transformed. In $\mathbf{q}$ = (q_x,q_y) space, the transformed intensity was radially averaged with $q = (q_x^2 + q_y^2)^{1/2}$. The ensemble average was taken over all frames separated by Δt, giving $D(q,\Delta t)$. At minimum, 100 image differences contributed to each average to ensure adequate statistics.

For each q value, $D(q,\Delta t)$ is fit to match the form in eqn (6) with $A(q)$, $B(q)$ and $\tau(q)$ as fitting parameters using MATLAB's trust-region reflective fitting algorithm (see ESI† for a more

detailed description of the fitting procedure). Thresholds and initialization parameters were chosen to minimize fit rejection over the q range. Fits with R^2 correlation values less than 95% were excluded from further analysis of $\tau(q)$ to eliminate cases where eqn (6) did not fit the empirical $D(q,\Delta t)$. Fits that were rejected were nearly exclusively in regions of low q (typically $q < 0.2\ \mu m^{-1}$) where the video was too short for the image structure function to reach an appreciable plateau, and in regions of high q (typically $q > 3\ \mu m^{-1}$) where the frame rate was too slow to measure dynamics.

In order to directly evaluate the accuracy of measuring the motion of dilute particles using d-DDM, multiple particle tracking microrheology was used to analyse the same videos used for DDM. A more detailed description of the algorithms used for multiple particle tracking, a widely employed technique, can be found elsewhere.[1–3] Briefly, MPT extracts particle dynamics by first isolating the center of distinct particles to subpixel resolution in each frame of a video. As the particles move from frame to frame, their centers displace. Linking centers of the same particle between frames forms a particle trajectory, from which the displacement of each particle can be calculated as a function of time step Δt. For Brownian motion of non-interacting particles, the ensemble-averaged mean squared displacement is related to Δt by

$$\langle r_{2D}{}^2(\Delta t)\rangle = \left(4\lambda^2 - \frac{4}{3}D_{Self}t_E\right) + 4D_{Self}\Delta t \qquad (39)$$

where D_{Self} is the particle self-diffusivity, λ the localization error, and t_E the exposure time.[39,40] Particle isolation and trajectory construction were performed in MATLAB using algorithms made freely available by Kilfoil and coworkers.[41] In these algorithms, thresholds for distinct particles, including both the maximum diameter and minimum intensity of the particle are chosen by the user to minimize effects of static and dynamic particle tracking error. Diffusivities were extracted by fitting the measured mean squared displacement to eqn (39) and calculating the localization uncertainty according to the methods described by Michalet.[39,40]

Results and discussion

Analyzing simulated micrographs using DDM

To test the accuracy of using the LSI decomposition analysis in a controlled LSV imaging system, we simulated micrograph series of particles undergoing 2D Brownian random walks in different illumination systems. Fig. 5 shows the simulated illumination systems and micrograph series. Three illumination systems were studied: (1) a LSI imaging system where $\alpha = 255$ across the entire image; (2) an LSV imaging system with a linear gradient in α in one dimension; and (3) an LSV imaging system with radially symmetric α variation. These three systems closely resemble what is observed experimentally in fluorescence microscopy, dark-field microscopy at high magnification, and dark-field microscopy at low magnification, respectively.

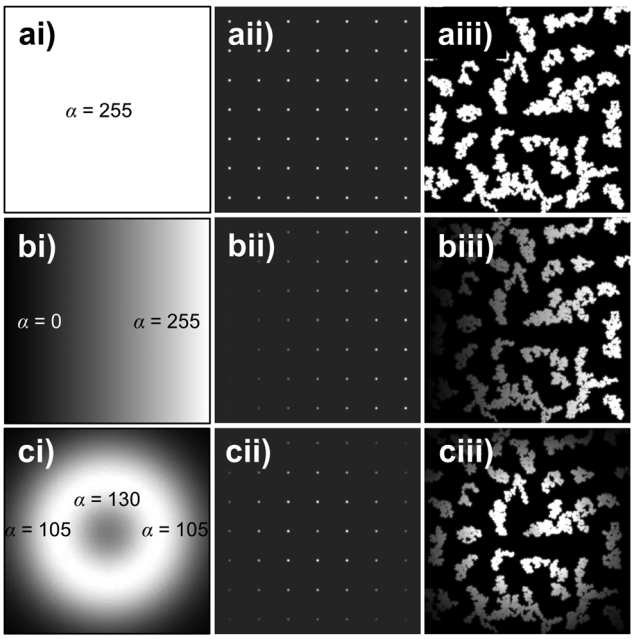

Fig. 5 Brownian motion simulations in LSI and LSV imaging systems. Rows correspond to three different illumination systems. Row (a) control, LSI where $\chi = 0$. Row (b) LSV imaging system where $\chi = 5 \times 10^{-3}$ pix^{-1}. Row (c) LSV imaging system with $\chi = 6 \times 10^{-3}$ pix^{-1}. Columns correspond to aspects of the simulation. (i) Spatial dependence of the magnitude of the particle intensity, α. (ii) Particles at $t = 0$. (iii) Particle trajectories.

Fig. 6 shows select q of $D(q,\Delta t)$ for each of the simulated micrograph series. Substituting eqn (38) into eqn (16) and (29) gives the analytical equations of $D(q,\Delta t)$ for a single particle undergoing Brownian motion in LSI and LSV imaging systems respectively.

$$D(\mathbf{q},\Delta t)_{LSI} = 2\sigma^4 e^{-\sigma^2 q^2}\langle\alpha^2(\mathbf{x}_0)\rangle[1 - e^{-D_{Self}q^2\Delta t}] \qquad (40)$$

$$D(\mathbf{q},\Delta t)_{LSV} = 2\sigma^4 e^{-\sigma^2 q^2}\langle\alpha^2(\mathbf{x}_0)\rangle[1 - e^{-D_{Self}q^2\Delta t} + \chi^2 D_{Self}\Delta t] \qquad (41)$$

These functions are plotted (multiplied by the number of particles simulated but with no other adjustable parameters) along with the measured $D(q,\Delta t)$ in Fig. 6. As seen in Fig. 6, both the LSI and LSV functions quantitatively match the simulated $D(q,\Delta t)$ for Δt corresponding to those typically observed in experiments. The effects of LSV are barely perceivable in the simulated signal, and are only noticeable in the analytic function after multiple orders of additional time magnitude. Since the functional forms of $\alpha(\mathbf{x}_i)$ in the simulations were specifically chosen to accurately represent the experimental system, these results suggest that in analyzing the experimental micrographs and image structure functions, it is reasonable to use the LSI decomposition in place of the LSV decomposition without any significant loss of accuracy, *e.g.*, for cases where χ cannot be directly measured. Simulations conducted for much longer time than required to extract the diffusivity (Fig. S4, ESI†) indeed show an increase in $D(q,\Delta t)$ (Fig. S5, ESI†) at long times that is modeled by eqn (41), illustrating that it captures the first-order effects of LSV well.

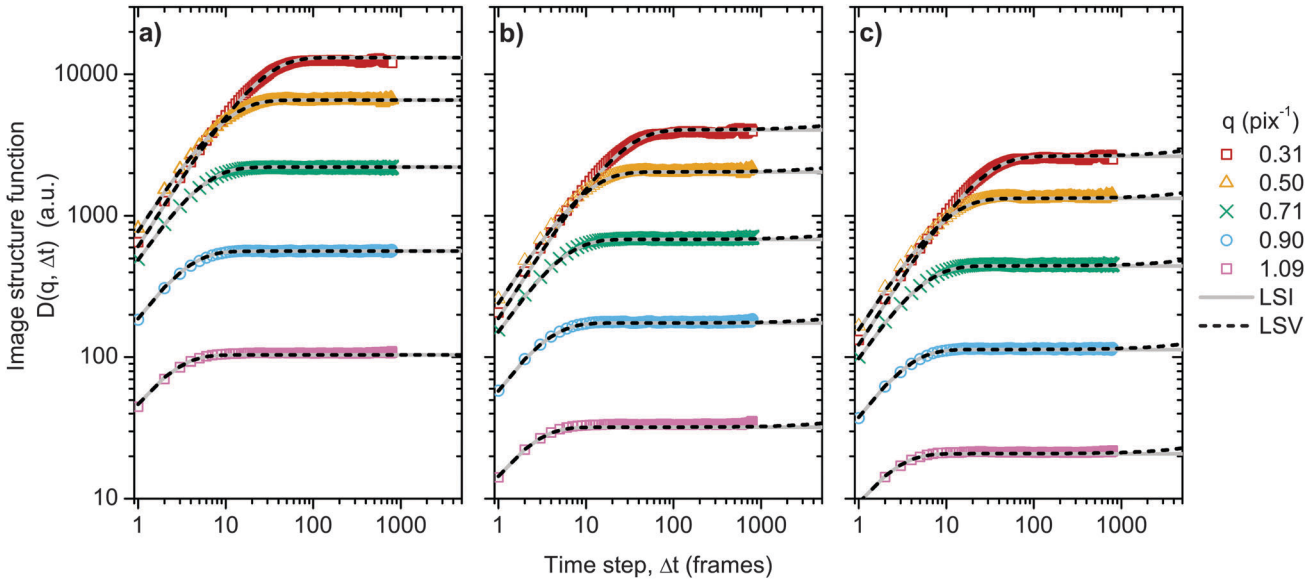

Fig. 6 Analyzing the image structure function of simulated micrographs. The calculated image structure functions in (a), (b), and (c) correspond to simulations (a), (b), and (c) in Fig. 5. Dashed and solid lines correspond to the analytical LSV (eqn (41)) and LSI (eqn (40)) functions for Gaussian particles respectively.

Measuring the diffusivity of optically dilute Au nanoparticles

To test the accuracy of using the LSI decomposition analysis in a real LSV experimental system, we imaged Au nanoparticles diffusing in viscous sucrose solutions under dark-field microscopy. We then compared the diffusivity measured *via* DDM analysis and MPT analysis of the micrographs. Fig. 7 shows the linear space variance in the experimental system and the micrographs collected. Au nanoparticles produce different intensity profiles under different magnifications: Gaussian profiles are observed under 10× magnification and profiles reminiscent of Bessel–Gaussian beams are observed under 40× magnification. Notably, the mechanics of DDM is identical during analysis of the two magnifications since it conveniently requires no knowledge of the scatterer intensity profiles *a priori*.

Fig. 1d provides one example of the image structure function calculated from the dark-field micrographs at 10× magnification.

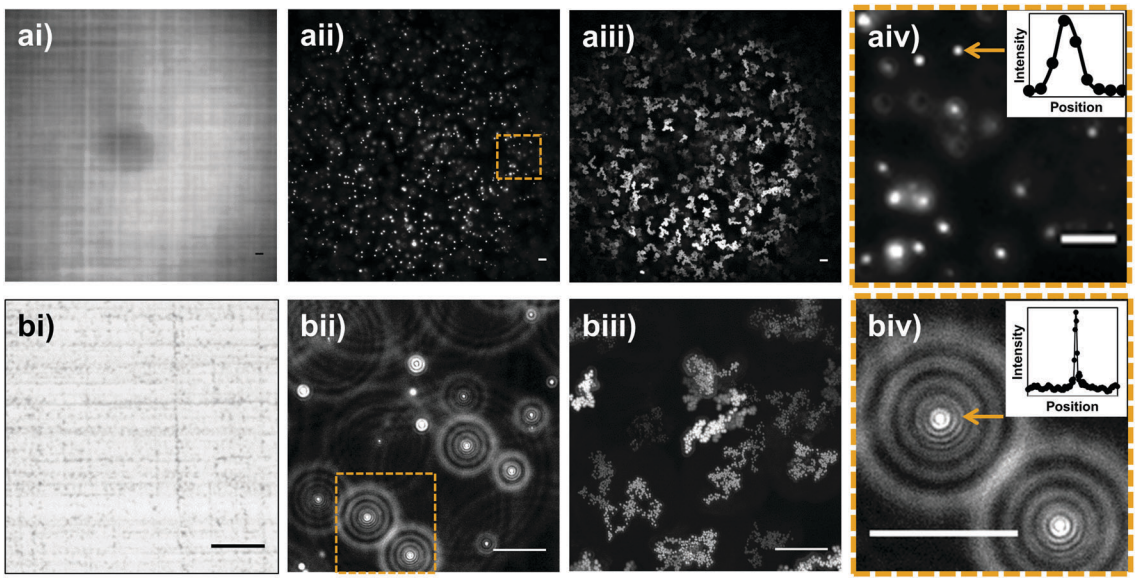

Fig. 7 Imaging the movement of Au nanoparticles dispersed in 40 wt% sucrose solutions using dark-field microscopy. Row (a) corresponds to 10× magnification; (b) corresponds to 40× magnification. (i) Spatial dependence of the magnitude of the particle intensity. (ii) Individual micrograph. (iii) Projection of the maximum intensity of each frame of the micrograph video gives the particle trajectories. (iv) Closer examination of the micrographs in (ii) show that nanoparticles produce Gaussian intensity profiles (inset) present under 10× magnification and Bessel–Gaussian beam-like intensity profiles (inset) under 40× magnification. All scale bars are 10 μm.

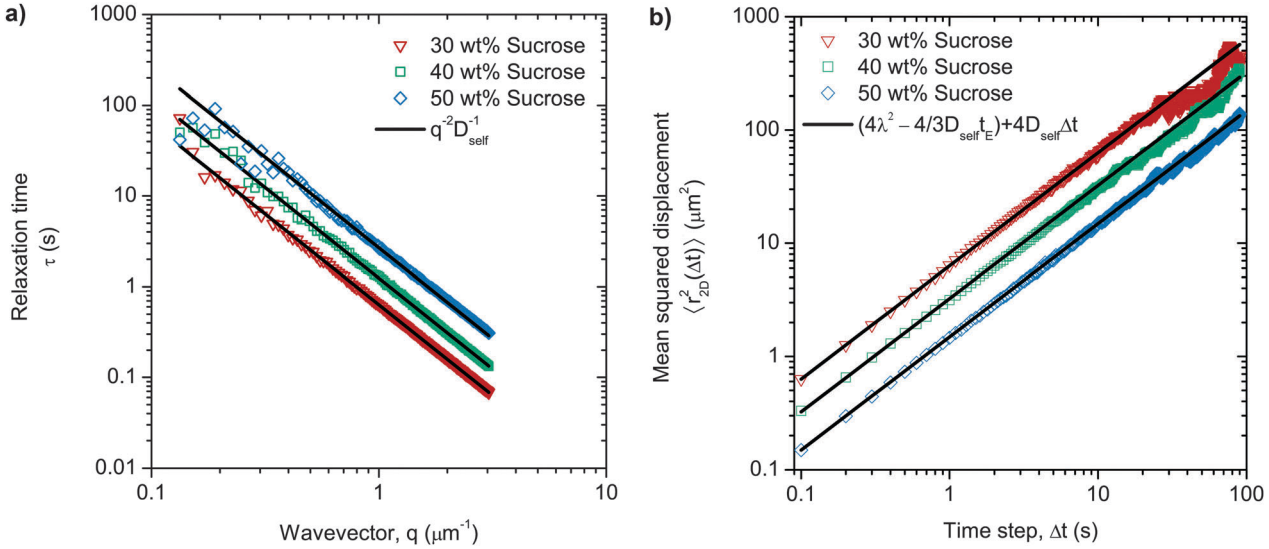

Fig. 8 Measuring nanoparticle diffusivity *via* dark-field DDM and multiple particle tracking (10× magnification). (a) Relaxation time $\tau(q)$ as a function of wavevector q for 100 nm Au NP sucrose dispersions. Error bars in τ are smaller than the markers. (b) Mean squared displacements of tracked 100 nm Au NPs. Noise in $\langle r_{2D}{}^2(\Delta t)\rangle$ at large Δt is due to the smaller number of trajectories that contribute to the average.

As expected based on the theoretical and simulation analysis, the LSI decomposition fits the measured values well over the course of the micrograph series. Fitting $D(q,\Delta t)$ to eqn (6) gives the relaxation time, τ as a function of q. The same is seen for the image structure functions calculated from micrographs at 40× magnification (see Fig. S6a, ESI†).

Fig. 8a and b give the material relaxation time obtained from DDM and the mean squared displacement obtained from MPT in each of the three sucrose solutions respectively. The material relaxation time decreases as q^{-2} as predicted for Brownian motion in all samples. The mean squared displacement is linearly proportional to Δt as expected for Brownian motion. The diffusivities of the particles are measured by fitting τ and $\langle r_{2D}{}^2(\Delta t)\rangle$ to eqn (17) and (39) respectively. Table 1 gives the average diffusivity extracted from the dark-field micrographs. We see good quantitative agreement between the diffusivities calculated from DDM and MPT for single movies, thus validating the use of LSI DDM analysis in LSV imaging systems for sufficiently small χ.

It is interesting to note the differences in error of the diffusivity calculated at the two different magnifications in Table 1. Specifically, the errors in DDM at 10× magnification are generally lower than the errors at 40× magnification. This reflects the fact that a larger population contributes to the ensemble at a low magnification. In DDM, not only do more particles contribute to the intensity fluctuations at higher magnification, but additionally the analysis samples the statistically valid q range (0.2–3 μm^{-1}) at a higher frequency. This can easily seen by the larger number of $\tau(q)$ data points present in Fig. 8a compared to those in Fig. S6b (ESI†).

By contrast, in MPT analysis, low magnification contributes both beneficially and detrimentally to the measurement error. On one hand, more particles are tracked at the low magnification, which improves the statistics of the mean squared displacements at long times (which is observed when comparing Fig. 8b to Fig. S6c, ESI†). On the other hand, there is greater error in the localization accuracy of the particle tracking algorithm, thereby increasing both the static and dynamic tracking error, which corrupts the mean squared displacement at short times.[39,40] From a computational standpoint, the computation time of MPT scales like $\sim e^N$, where N is the number of particles tracked, such that the computation time increases considerably at lower magnification in order to achieve greater statistical precision.

Table 1 Diffusivities of optically dilute 100 nm Au nanoparticles in aqueous sucrose solutions measured using d-DDM and MPT

		Diffusivity ($\mu m^2\ s^{-1}$)		
Magnification	Method	30 wt%	40 wt%	50 wt%
10×	d-DDM[a]	1.5809 ± 0.0006	0.8070 ± 0.0006	0.373 ± 0.001
	MPT[b]	1.58 ± 0.01	0.811 ± 0.005	0.372 ± 0.002
	Stokes–Einstein[c]	1.50 ± 0.20	0.746 ± 0.099	0.307 ± 0.041
40×	d-DDM[a]	1.56 ± 0.01	0.803 ± 0.005	0.3636 ± 0.0008
	MPT[b]	1.56 ± 0.05	0.82 ± 0.02	0.368 ± 0.007
	Stokes–Einstein[c]	1.54 ± 0.20	0.757 ± 0.100	0.312 ± 0.041

[a] σ_{DDM} calculated from scatter in $\tau(q)$. [b] σ_{MPT} calculated using methods developed by Michalet.[39] [c] $\sigma_{Stokes-Einstein}$ calculated based on Au NP polydispersity (dia = 94.6 ± 12.5 nm) and error in ambient temperature measurement (±0.2 °C).

However, the computational time to conduct DDM is identical for all magnifications. The absolute computational times of the two methods depends on a multitude of factors (*e.g.* in DDM, algorithms used, whether parallelization is employed,[21] the dimensions of the image; in MPT, algorithm used, displacement of particles between frames, number of particles tracked); as such, it is difficult to generalize whether one method is faster than the other for all systems.

From this observation and discussion, we surmise that DDM can be used to obtain potentially better statistics compared to MPT, and moreover that improved statistical accuracy of DDM can be obtained by switching to lower magnifications without incurring any additional computational time. What remains to be seen, however, is whether the absolute error is smaller using MPT or DDM. In this work, we used an *ad hoc* method to calculate error of the measured diffusivity (inversion of the multi-parameter Jacobian fit matrix). In light of the extensive work that has been done[39,40] to understand static and localization uncertainty in calculating the simple Brownian diffusivity of particles using MPT, it is likely that calculation of the true diffusivity error using DDM is as (if not more) complex as calculating the error from MPT. Clearly, a more exhaustive error analysis needs to be completed to elucidate relative accuracy of the two techniques in the optically dilute limit.

Regardless of whether DDM or MPT is used to analyse the micrographs, dark-field micrograph videos provide a substantial improvement over bright-field micrograph videos. As illustrated in Fig. 1, dark-field micrographs of optically dilute gold nanoparticles dispersed in sucrose are substantially higher fidelity than bright-field micrographs of the same sample. The bright-field micrographs are of such low fidelity that distinct particle intensity profiles are not observed. Consequently, the particle tracking algorithms could not identify any particles within the micrograph series, rendering MPT useless.

Generally, one of the advantages of DDM is that it can be used to extract dynamic information from micrographs where distinct particle profiles are unobservable. Cerbino *et al.*[15] and He *et al.*[16] have demonstrated that it is possible to measure the diffusivities of 73 nm and 100 nm particles in Newtonian fluids by analysing bright-field speckle patterns with DDM. In these experiments, an exponential increase in $D(q,\Delta t)$ is observed if the volume fraction of particles is large enough to make $A(q)$ sufficiently greater than $B(q)$.[16] Since our dispersions ($\phi \sim 10^{-8}$) are more dilute than those previously studied[15,16] ($\phi \sim 10^{-2}$ and $\phi \sim 10^{-6}$ respectively), the collective intensity fluctuations due to particle movement are negligible compared to the background noise. $D(q,\Delta t)$, dominated by $B(q)$, therefore has no time dependence as seen in Fig. 1d. This low concentration effect is ameliorated through the use of dark-field imaging; $|i(q)|_{\text{darkfield}}^2 \gg |i(q)|_{\text{brightfield}}^2$, making $A(q)/B(q)$ sufficiently high even at low particle concentrations. Representative plots of $A(q)$ and $B(q)$ for the dark-field experiments are given in Fig. S7 (ESI†).

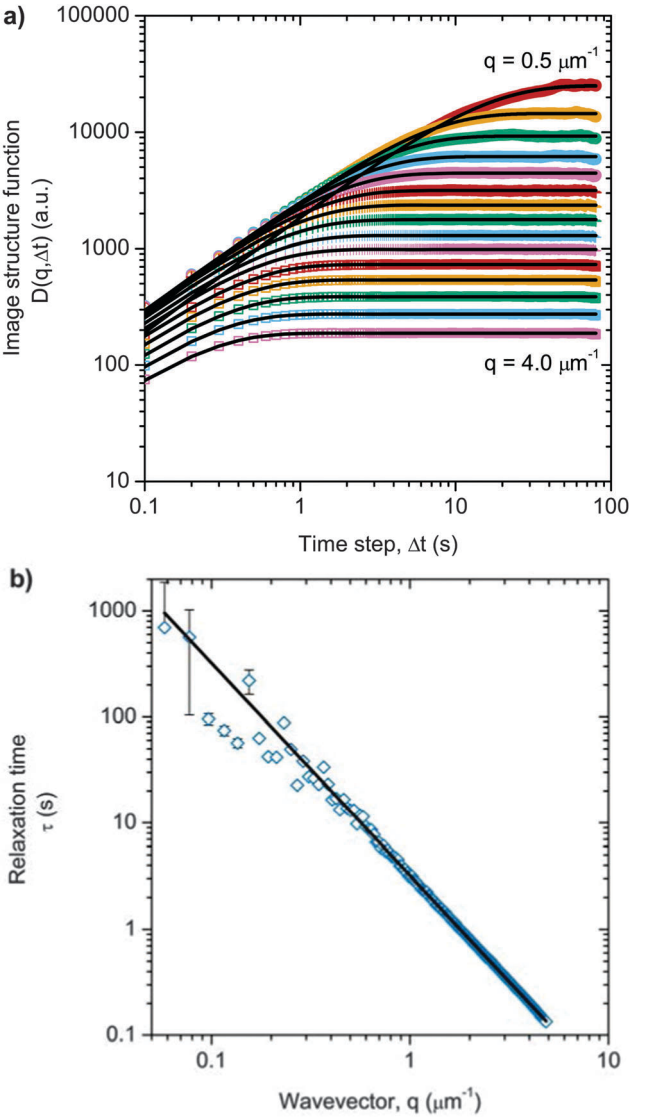

Fig. 10 Dark-DDM of optically dense micrographs. (a) The measured image structure function displays the classic exponential plateau expected for Brownian motion. Solid lines designate LSI fits. (b) Relaxation time $\tau(q)$ (◇) as a function of wavevector q obtained from linear space invariance fit. Solid line designates fit to q^{-2}. Error bars in τ are smaller than the markers for $q > 0.16$ μm^{-1}.

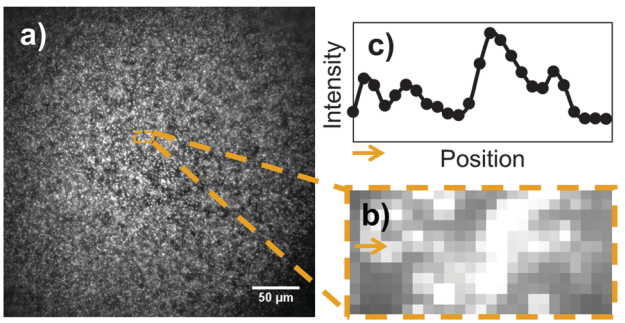

Fig. 9 Optically dense dark-field micrographs. (a) Dark-field micrograph of 100 nm Au nanoparticles in 50 wt% sucrose solutions at a hydrodynamically dilute volume fraction, $\phi = 3.2 \times 10^{-5}$. (b) Close-up of a portion of the micrograph. Arrow designates a row of pixels whose intensity is plotted in (c). The close proximity of the intensity profiles prevents accurate particle tracking required in multiple particle tracking microrheology.

Measuring the diffusivity of optically dense Au nanoparticles

To further illustrate the utility of dark-field DDM, we measured the diffusivity of Au nanoparticles that produce optically dense micrographs. At a volume fraction of 3.2×10^{-3} vol%, the optically dense dispersion is still physically dilute in the sense that it is expected that the nanoparticles do not interact hydrodynamically and therefore undergo independent Brownian motion. However, at this concentration, they are optically dense in that it is impossible to distinguish individual particles within a dark-field micrograph. Fig. 9 shows a dark-field micrograph of this sample. Examining the intensity profile (Fig. 9c) across one small portion of the micrograph further illustrates that the intensity contributions from individual particles are indistinguishable. As such, it is not possible to perform traditional MPT on this micrograph to measure particle diffusivity. It is possible, however, to measure the diffusivity using DDM.

Using the techniques developed here, DDM overcomes the limitations of MPT in analysing the optically dense samples. Fig. 10a shows the image structure function of the optically dense sample. As expected, it displays the expected exponential approach to a plateau characteristic of Brownian motion. Fitting $D(q,\Delta t)$ to eqn (6) gives the relaxation time, τ as a function of q which is plotted in Fig. 10b. The diffusivity measured from the relaxation time is 0.3115 ± 0.0006 μm^2 s^{-1}. The Stokes–Einstein diffusivity calculated from the diameter of the nanoparticles measured by TEM is $D_{ES} = 0.32 \pm 0.04$ μm^2 s^{-1}. The close agreement suggests that (1) dark-DDM successfully measures the diffusivity for optically dense samples and (2) dark-DDM can be used to measure the hydrodynamic radius of a nanoparticle in solution if the suspending medium viscosity is known.

Conclusions

We have demonstrated that differential dynamic analysis can be applied to dark-field micrographs to extract dynamic information in a similar manner as other imaging modes, illustrated here for nanoparticle dispersions. By recasting the fundamental framework of DDM in a particle-displacement approach, we showed that in linear space variant illumination systems, the image structure function $D(\mathbf{q},\Delta t)$ can be approximated by four sub-functions: $A(\mathbf{q})$, $g(\mathbf{q},\Delta t)$, $B(\mathbf{q})$ and $V(\mathbf{q},\Delta t)$. $V(\mathbf{q},\Delta t)$ accounts for the contributions due to linear space variance, while the others are identical to the linear space invariant analogues. We note that the theoretical treatment developed here is equally valid for any imaging system that produces a non-uniform optical illumination field. As such, we anticipate that our results should be applicable to other imaging modes not yet explored by DDM, such as total internal reflectance microscopy[42,43] or Brewster angle microscopy.[44,45]

Most importantly, our results show that DDM is quite robust to the type and uniformity of illumination, provided that the length scale for gradients in the illumination is small relative to the probing length scale of DDM. For the specific case of Brownian motion, our theoretical analysis suggests that in the limit where the LSV length scale $\chi \ll q$, $V(\mathbf{q},\Delta t)$ is significantly less than the autocorrelation function $g(\mathbf{q},\Delta t)$. In this case, traditional LSI decomposition analysis can be used to analyse dark-field micrographs. This claim was verified by conducting simple simulations in different idealized illumination systems and by experimentally measuring the diffusivity of Au nanoparticles in sucrose solutions.

It is likely that different types of dynamics will result in different forms of $V(\mathbf{q},\Delta t)$ such that its dependence on the $\alpha(\mathbf{x}_i)$ field has a significant effect on the image structure function, unlike in the case of Brownian motion case discussed. However, using the framework presented here, it is possible to derive $V(\mathbf{q},\Delta t)$ for different types of dynamics by simply replacing the probability distribution of displacements $p(\delta\mathbf{x},\Delta t)$ with an appropriate model for the dynamics and subsequently determine whether the measured signal needs to be fit to different functions to obtain accurate fitting and interpretation of $D(\mathbf{q},\Delta t)$.

The utility of dark-field DDM was illustrated by measuring the diffusivity of Au nanoparticles in an optically dense solution where more traditional MPT analysis fails. Furthermore, it appears that DDM may provide reduced error compared to MPT with regards to obtaining accurate diffusivity measurements, and with greatly reduced computational cost. Additionally, comparing DDM analysis of bright-field micrographs of the same sample illustrates that dark-DDM has a better signal-to-noise ratio than bright-DDM. Given these benefits, we anticipate that dark-field DDM could become a preferred method for characterizing the dynamics of complex fluids whose features lie below the optical limit in conventional projection imaging, but whose dynamical fluctuations are still measurable in their scattering.

Acknowledgements

AVB was supported by the National Science Foundation Graduate Research Fellowship under Grant No. DGE1144085. Any opinion, findings, and conclusions or recommendations expressed in this material are those of the authors and do not necessarily reflect the views of the National Science Foundation. AVB and TMS were funded in part under Award No. CBET 1438779. MEH was funded in part by the National Science Foundation under Award No. CBET 1351371.

References

1 J. Crocker and D. Grier, *J. Colloid Interface Sci.*, 1996, **179**, 298–310.
2 T. G. Mason, K. Ganesan, J. van Zanten, D. Wirtz and S. Kuo, *Phys. Rev. Lett.*, 1997, **79**, 3282–3285.
3 T. M. Squires and T. G. Mason, *Annu. Rev. Fluid Mech.*, 2010, **42**, 413–438.
4 M. Raffel, C. E. Willert, S. Wereley and J. Kompenhans, *Particle Image Velocimetry: A Practical Guide*, Springer-Verlag, Berlin Heidelberg, 2nd edn, 2007.
5 R. J. Adrian, *Exp. Fluids*, 2005, **39**, 159–169.
6 A. Melling, *Meas. Sci. Technol.*, 1997, **8**, 1406–1416.

7 D. J. Pine, D. A. Weitz, P. Chaikin and E. Herbolzheimer, *Phys. Rev. Lett.*, 1988, **60**, 1134–1137.
8 D. J. Pine, D. A. Weitz, J. X. Zhu and E. Herbolzheimer, *J. Phys. France*, 1990, **51**, 2101–2127.
9 E. L. Elson and D. Magde, *Biopolymers*, 1974, **13**, 1–27.
10 D. Magde, E. L. Elson and W. W. Webb, *Biopolymers*, 1974, **13**, 29–61.
11 B. J. Berne and R. Pecora, *Dynamic Light Scattering: With Applications to Chemistry, Biology, and Physics*, Dover Publications, Inc., Mineola, NY, The Dover edn, 2000.
12 H. Auweter and D. Horn, *J. Colloid Interface Sci.*, 1985, **105**, 399–409.
13 F. Giavazzi and R. Cerbino, *J. Opt.*, 2014, **16**, 083001.
14 S. Buzzaccaro, M. D. Alaimo, E. Secchi and R. Piazza, *J. Phys.: Condens. Matter*, 2015, **27**, 194120.
15 R. Cerbino and V. Trappe, *Phys. Rev. Lett.*, 2008, **100**, 188102.
16 K. He, M. Spannuth, J. C. Conrad and R. Krishnamoorti, *Soft Matter*, 2012, **8**, 11933–11938.
17 M. Dienerowitz, M. Lee, G. Gibson and M. Padgett, *Lab Chip*, 2013, **13**, 2359–2363.
18 F. Ferri, A. D'Angelo, M. Lee, A. Lotti, M. C. Pigazzini, K. Singh and R. Cerbino, *Eur. Phys. J.: Spec. Top.*, 2011, **199**, 139–148.
19 Y. Gao, J. Kim and M. E. Helgeson, *Soft Matter*, 2015, **11**, 6360–6370.
20 L. G. Wilson, V. A. Martinez, J. Schwarz-Linek, J. Tailleur, G. Bryant, P. N. Pusey and W. C. K. Poon, *Phys. Rev. Lett.*, 2011, **106**, 018101.
21 P. J. Lu, F. Giavazzi, T. E. Angelini, E. Zaccarelli, F. Jargstorff, A. B. Schofield, J. N. Wilking, M. B. Romanowsky, D. A. Weitz and R. Cerbino, *Phys. Rev. Lett.*, 2012, **108**, 218103.
22 R. Colin, R. Zhang and L. G. Wilson, *J. R. Soc., Interface*, 2014, **11**, 20140486.
23 V. A. Martinez, R. Besseling, O. A. Croze, J. Tailleur, M. Reufer, J. Schwarz-Linek, L. G. Wilson, M. A. Bees and W. C. K. Poon, *Biophys. J.*, 2012, **103**, 1637–1647.
24 F. Giavazzi, S. Crotti, A. Speciale, F. Serra, G. Zanchetta, V. Trappe, M. Buscaglia, T. Bellini and R. Cerbino, *Soft Matter*, 2014, **10**, 3938–3949.
25 M. Reufer, V. A. Martinez, P. Schurtenberger and W. C. K. Poon, *Langmuir*, 2012, **28**, 4618–4624.
26 Y. Gao and M. E. Helgeson, *Opt. Express*, 2014, **22**, 10046–10063.
27 F. Giavazzi, D. Brogioli, V. Trappe, T. Bellini and R. Cerbino, *Phys. Rev. E: Stat., Nonlinear, Soft Matter Phys.*, 2009, **80**, 031403.
28 F. Croccolo, F. Scheffold and H. Bataller, *C. R. Mec.*, 2013, **341**, 378–385.
29 T. Horio and H. Hotani, *Nature*, 1986, **321**, 605–607.
30 G. A. Jamjoom, *J. Clin. Microbiol.*, 1983, **17**, 717–721.
31 R. M. Macnab, *J. Clin. Microbiol.*, 1976, **4**, 258–265.
32 A. M. van der Zande, P. Y. Huang, D. A. Chenet, T. C. Berkelbach, Y. You, G.-H. Lee, T. F. Heinz, D. R. Reichman, D. A. Muller and J. C. Hone, *Nat. Mater.*, 2013, **12**, 554–561.
33 M. Hu, C. Novo, A. Funston, H. Wang, H. Staleva, S. Zou, P. Mulvaney, Y. Xia and G. V. Hartland, *J. Mater. Chem.*, 2008, **18**, 1949–1960.
34 K. A. Willets and R. P. Van Duyne, *Annu. Rev. Phys. Chem.*, 2007, **58**, 267–297.
35 I. Nemoto, *J. Opt. Soc. Am. A*, 1988, **5**, 1848–1851.
36 N. Streibl, *J. Opt. Soc. Am. A*, 1985, **2**, 121–127.
37 W. Feller, *An Introduction to Probability Theory and Its Application*, 3rd edn, 1967.
38 The MATLAB code used for DDM analysis and fitting of Brownian diffusivities is available for non-profit distribution and use from the author's website http://engineering.ucsb.edu/~helgeson/ddm.html.
39 X. Michalet, *Phys. Rev. E: Stat., Nonlinear, Soft Matter Phys.*, 2010, **82**, 059904.
40 T. Savin and P. S. Doyle, *Biophys. J.*, 2005, **88**, 623–638.
41 M. L. Kilfoil, http://people.umass.edu/kilfoil/downloads.html, 2015.
42 H.-J. Wu and M. A. Bevan, *Langmuir*, 2005, 1244–1254.
43 M. A. Bevan and D. C. Prieve, *Langmuir*, 1999, **15**, 7925–7936.
44 M. C. Friedenberg, G. G. Fuller, C. W. Frank and C. R. Robertson, *Langmuir*, 1994, **10**, 1251–1256.
45 M. M. Lipp, K. Y. C. Lee, J. A. Zasadzinski and A. J. Waring, *Rev. Sci. Instrum.*, 1997, **68**, 2574–2582.

